Direct numerical simulation of electroconvective instability and hysteretic current-voltage response of a permselective membrane

Van Sang Pham,[1] Zirui Li,[2,3] Kian Meng Lim,[1,4] Jacob K. White,[5] and Jongyoon Han[3,5,6]

[1]*Singapore-MIT Alliance, National University of Singapore, Singapore*

[2]*College of Mechanical and Electrical Engineering, Wenzhou University, China*

[3]*Singapore-MIT Alliance for Research and Technology (SMART) Centre, Singapore*

[4]*Department of Mechanical Engineering, National University of Singapore, Singapore*

[5]*Department of Electrical Engineering and Computer Science, Massachusetts Institute of Technology, 77 Massachusetts Avenue, Cambridge, Massachusetts 02139, USA*

[6]*Department of Biological Engineering, Massachusetts Institute of Technology, 77 Massachusetts Avenue, Cambridge, Massachusetts 02139, USA*

(Received 31 July 2012; revised manuscript received 24 September 2012; published 11 October 2012)

We present a systematic, multiscale, fully detailed numerical modeling for dynamics of fluid flow and ion transport covering Ohmic, limiting, and overlimiting current regimes in conductance of ion-selective membrane. By numerically solving the Poisson-Nernst-Planck-Navier-Stokes equations, it is demonstrated that the electroconvective instability, arising from the electric field acting upon the extended space charge layer, and the induced strong vortical fluid flow are the dominant factors of the overlimiting current in the planar membrane system. More importantly, at the transition between the limiting and the overlimiting current regimes, hysteresis of electric current is identified. The hysteresis demonstrates the important role of the electroconvective flow in enhancing of current in electrolyte systems with ion-selective membrane.

DOI: 10.1103/PhysRevE.86.046310 PACS number(s): 47.20.−k, 82.40.Bj, 82.45.−h, 82.39.Wj

I. INTRODUCTION

Ion-selective membraness are widely used in many engineering applications, such as water desalination, fuel cells, and blood analysis, etc. Operational efficiency of a conducting ion-selective membrane is characterized by its current-voltage (I-V) curve. As depicted in Fig. 1, a typical I-V curve consists of three distinct regimes: a low current Ohmic regime, a plateau-limiting regime, and an overlimiting current regime. While the first two regimes could be explained by the classical theory of concentration polarization [1,2], the mechanism for the third regime was unclear for a long time. So far, one of the most promising mechanisms for the overlimiting current is the fluid convection caused by electro-osmotic slip of the second kind, suggested by Rubinstein and Zaltzman [3,4]. Such electro-osmotic slip at the membrane surface yields instability of the quiescent concentration polarization region and generates an electroconvective flow that manifests paired vortices. This vortical flow destroys the diffusion layer, and brings more ions to the membrane surface to produce an overlimiting conductivity. This mechanism is supported by a number of experimental studies. Kim and co-workers reported a visualization of strong nonequilibrium electro-osmotic vortices in the overlimiting current regime of a nanochannel array proving the existence of the second kind electro-osmosis and vortical flow on a flat permselective membrane [5]. The first direct experimental verification of the electro-osmotic instability was conducted by Rubinstein *et al*. [6]. It was reported that, when a significantly high electric field is applied across a flat cation-selective membrane, vortical flow appears near the membrane surface; concurrently, the electric current passing through the system exceeds the limiting-current value. Additional direct experimental evidence for the electro-osmotic instability was reported by Yossifon and Chang [7] who demonstrated that the vortex pairs appearing near nanoslot are due to the instability of the space charge layer. The mechanism was also supported indirectly by the experimental observation [8] where overlimiting current disappeared as the fluid convection is suppressed by using a high viscosity solution.

The electro-osmotic slip of the second kind was first introduced by Dukhin *et al*. [9]. Subsequently, Rubinstein and Zaltzman [3,4] proposed that such a nonlinear electrokinetic slip on a flat permselective membrane surface could explain ion transport in the overlimiting current regime. However, clear understanding and modeling of this phenomenon would require an accurate calculation of the ion concentrations, residual space charge, local electric field, and the fluid flow near the ion-selective membrane, which is a numerically expensive, coupled, and multiscale problem. Demekhin and co-workers [10] recently reported a simulation work on electroconvection in electrolyte for this problem. By decoupling the nonlinear Poisson-Nernst-Planck (PNP) equations, and ignoring the inertial term in the Navier-Stokes (NS) equations, they demonstrated the existence of electrokinetic instability of electrolyte near a permselective membrane.

In this paper, we study the electroconvection near a permselective membrane by accurately solving the full PNP and NS equations. Unlike Demekhin's method, the PNP equations are not decoupled in this work, and the inertial term in the NS equations will be considered accurately. The I-V curve will be considered under the context of electroconvection. We will examine in detail the formation and development of electroconvective instability over the membrane surface. Details of the transition between different current regimes will be also revealed. Importantly, we will show that the electroconvection system exhibits a hysteretic characteristic in the transition between the limiting and overlimiting regimes.

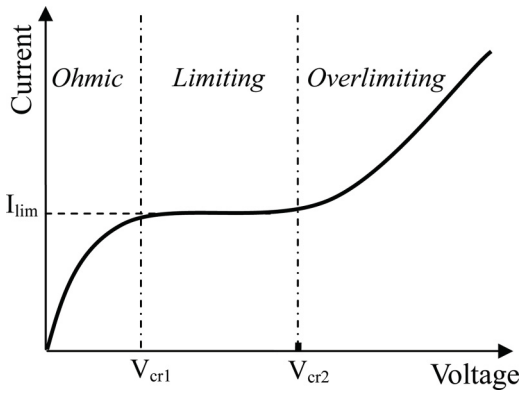

FIG. 1. Sketch of a typical current-voltage (I-V) curve of a permselective membrane.

The hysteresis provides important insights into the mechanism behind this transition.

II. FORMULATION

We consider a model system of a permselective membrane interfacing with a symmetric, binary electrolyte solution. The bulk space is assumed at a distance l_0 from the membrane, where the concentrations of the anions and cations are maintained at bulk concentration $C_{\rm Bulk}$. Electric current is driven through the membrane by a bias voltage between the bulk space and the membrane. To mimic macroscopic flat membrane surface with microscale variations, the membrane is modeled by a series of wavy cation-selective surfaces as sketched in Fig. 2, where the amplitude of the wave is purposely chosen to be very small (e.g., 0.001 times the wavelength). This variation in membrane surface produces a periodical electric field that generates a perturbative fluid motion when an external electric field is applied. Such a fluid flow perturbation is typically confined within the distance of $\sim O(a)$, and therefore does not lead to significant changes in ion transport in the Ohmic regime. However, in the overlimiting regime, this perturbation can lead to significant fluid instability and changes in both ion concentration and flux. This setup reflects the

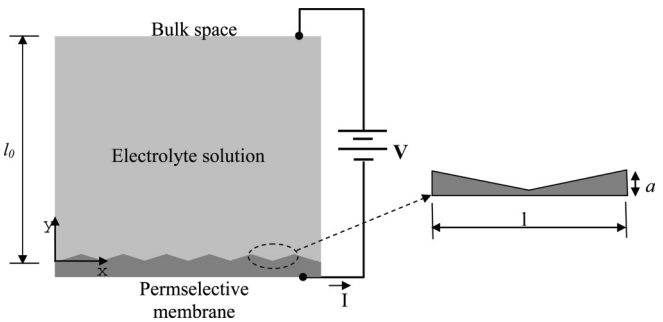

FIG. 2. Model system of a permselective membrane interfacing with an electrolyte. The membrane is modeled by a series of wavy cation-selective surfaces. The wave amplitude (a) is much smaller than the wavelength (l), e.g., $a = 0.001 \times l$. A bias voltage is applied between the membrane and bulk space to drive electric current through the membrane.

experimental situation, where micro- or submicroscale roughness of the membrane could act as the initiation point of fluid instability.

In the system, transport of ions is governed by the Nernst-Planck equations [Eqs. (1) and (2)]; electric potential field is related to the ion concentrations via the Poisson equation [Eqs. (3) and (4)]; and the fluid motion is governed by the Navier-Stokes equations [Eqs. (5) and (6)]. These equations are given in the dimensionless form as follows:

$$\frac{1}{\tilde{\lambda}_D}\frac{\partial \tilde{C}_\pm}{\partial \tilde{t}} = -\tilde{\nabla}\cdot\tilde{\mathbf{J}}_\pm, \tag{1}$$

$$\tilde{\mathbf{J}}_\pm = -\tilde{D}(\tilde{\nabla}\tilde{C}_\pm + Z_\pm\tilde{\nabla}\tilde{\Phi}) + \mathrm{Pe}\,\tilde{\mathbf{U}}\tilde{C}_\pm, \tag{2}$$

$$\tilde{\lambda}_D^2\tilde{\nabla}\cdot(\tilde{\nabla}\tilde{\Phi}) = -\tilde{\rho}_e, \tag{3}$$

$$\tilde{\rho}_e = Z_+\tilde{C}_+ + Z_-\tilde{C}_-, \tag{4}$$

$$\frac{1}{\mathrm{Sc}}\frac{1}{\tilde{\lambda}_D}\frac{\partial \tilde{\mathbf{U}}}{\partial \tilde{t}} = -\tilde{\nabla}\tilde{P} + \tilde{\nabla}^2\tilde{\mathbf{U}} - \mathrm{Re}(\tilde{\mathbf{U}}\cdot\tilde{\nabla})\tilde{\mathbf{U}} - \frac{1}{\tilde{\lambda}_D^2}\tilde{\rho}_e\tilde{\nabla}\tilde{\Phi}, \tag{5}$$

$$\tilde{\nabla}\cdot\tilde{\mathbf{U}} = 0, \tag{6}$$

where $\tilde{t}$, $\tilde{C}_\pm$, $\tilde{\Phi}$, $\tilde{\mathbf{U}}$, and $\tilde{P}$ denote the dimensionless time, concentration of cations ($+$) and anions ($-$), electric potential, vector of fluid velocity, and pressure, respectively. These quantities were normalized by the following reference values of time, ionic concentration, electric potential, velocity, and pressure, respectively:

$$\begin{aligned} &\tau_0 = \frac{l_0^2}{D_0}; \quad C_0 = C_{\rm Bulk}; \quad \Phi_0 = \frac{k_BT}{Ze}; \\ &U_0 = \frac{\varepsilon\Phi_0}{\eta l_0}; \quad P_0 = \frac{\eta U_0}{l_0}, \end{aligned} \tag{7}$$

where $C_{\rm Bulk}$ is the concentration of ions at the bulk space, l_0 is the characteristic length scale, $D_0 = (D_+ + D_-)/2$ is the average diffusivity, k_B is the Boltzmann constant, T is the absolute temperature, e is the elementary charge, $Z = |Z_\pm|$ is ion valence, η is the dynamics viscosity of solution, and ε is the permittivity of the solvent. Parameters $\tilde{D}_\pm = D_\pm/D_0$, $\tilde{\lambda}_D = \lambda_D/l_0$, and $\tilde{\rho}_e = \rho_e/C_{\rm Bulk}$ are dimensionless diffusion coefficients, the Debye length ($\lambda_D = \sqrt{\varepsilon k_BT/2C_{\rm Bulk}Z^2e^2}$), and the space charge, respectively. $\mathrm{Pe} = U_0l_0/D_0$, $\mathrm{Sc} = \eta/\rho_mD_0$, and $\mathrm{Re} = U_0l_0\rho_m/\eta$ are the Péclet number, the Schmidt number, and the Reynolds number, respectively.

The system is characterized by the dimensionless Debye length $\tilde{\lambda}_D$. In this study, $\tilde{\lambda}_D = 0.001$ corresponds to the characteristic length $l_0 = 13.8\ \mu$m, the bulk concentration $C_{\rm Bulk} = 0.5$ mM, and the absolute temperature $T = 300$ K. Other parameters used in the simulation include the diffusivities $D_+ = D_- = 10^{-9}$ m^2/s, the number of wavy surfaces $n_s = 20$, and the membrane length $l_m = 13.8\ \mu$m.

For closure of the governing equations, boundary conditions are also supplied. At the bulk space, ionic species are well mixed, $\tilde{C}_+ = \tilde{C}_- = 1$, and the fluid is stationary, $\tilde{\mathbf{U}} = 0$. At the membrane surface, no-flux condition is enforced to anions $\tilde{\mathbf{J}}_-\cdot\mathbf{n} = 0$; cations are assumed to be accumulated uniformly

at a concentration of $\tilde{C}_m$ ($\tilde{C}_+ = \tilde{C}_m = 2$); the common no-slip boundary condition is enforced to the fluid $\tilde{\mathbf{U}} = \mathbf{0}$. Bias voltage is applied to the system through a fixed-value boundary condition for electric potential at the bulk space ($\tilde{\Phi} = \mathbf{0}$) and the membrane ($\tilde{\Phi} = -V$). At other boundaries, all variables are assumed to be periodic.

III. NUMERICAL METHODS

The PNP and NS equations are nonlinearly coupled. These sets of equations relate to each other via the convection term in the PNP equations and the electric body force in the NS equations. Two major difficulties in solving numerically the PNP-NS equations are (i) the stiff nonlinear coupling of the PNP equations, especially occurring in the electrical double layer (EDL) of the permselective membrane where counterions strongly accumulate, and (ii) the rapid change of electrical body force field across the membrane's EDL where ions accumulate and the electric potential changes rapidly. A possible method to solve the PNP-NS equations is to discretize the fully coupled set of equations using the finite element method [11]. This approach, however, results in a large system of linear equations, which is computationally expensive. In contrast, the method proposed by Demekhin *et al*. [10] decouples the Poisson-Nernst-Planck equations and solves them sequentially. Although this method reduces the computational cost significantly, the accuracy might suffer in dealing with the strongly coupled equations.

In order to avoid solving the large system of linear equations and guarantee the strong coupling of the PNP equations, we developed a coupled method for solving the sets of PNP and NS equations. Starting with a velocity field from the previous iteration or initial condition, the potential and concentrations are simultaneously solved from the PNP equations. Then, electric body force is calculated and substituted into the NS equations. The velocity field obtained by solving the NS equations is substituted back into the PNP equations. The process is repeated until convergence is reached.

The finite volume method [12–14], which is locally conservative, is used for discretization of the equations. The nonlinear discretized PNP equations are solved using the Newton-Raphson method [15]. Due to the rapid variations of the ion concentrations and electric potential in the EDL, the mesh near the membrane is refined using the GMSH [16]. To avoid the nonlinear no-flux boundary condition of co-ions at the membrane, the primitive concentration variables $\tilde{C}_\pm$ are replaced by electrochemical potential variables $\mu_\pm = \ln \tilde{C}_\pm + Z_\pm \tilde{\Phi}$. In terms of the electrochemical potential variables, the ionic fluxes can be written as $\tilde{\mathbf{J}}_\pm = e^{\mu_\pm - Z_\pm \tilde{\Phi}}(-\tilde{D}_\pm \tilde{\nabla}\mu_\pm + \mathrm{Pe}\,\tilde{\mathbf{U}})$. Taking into account the no-slip boundary condition at the membrane surface, the no-flux boundary condition thus reduces to a simple zero-gradient boundary condition for the electrochemical potential variables. It is demonstrated that the equations involving $\mu_\pm$ require a lesser number of iterations in the Newton-Raphson method than the equations involving $C_\pm$ [17]. In addition, using the generalized minimal residual method [18,19], the discretized linear equations in terms of electrochemical potential are solved faster than that in terms of the primitive variables [17].

In the finite volume method, the NS equations can be solved separately or simultaneously [12,14]. In the flow developed near the permselective membrane, the body force varying dramatically in the membrane's EDL causes large pressure gradient in the normal direction of the surface. In order to guarantee coupling of the pressure and velocity, the NS equations are solved in a coupled manner in which all equations are solved simultaneously [17]. The Rhie-Chow interpolation [20] is used to derive an explicit equation for the pressure.

IV. RESULTS AND DISCUSSION

A. Current-voltage response of permselective membrane

By conducting simulations for different bias voltages, we examine the development of electroconvection flow and its effects on the distribution of ions and current passing through the membrane.

1. Ohmic regime—Ion concentration near membrane reduces with increasing bias voltage

We begin by applying a small bias voltage between the bulk space and the membrane to establish an electric field orthogonal to the membrane. Driven by the electric field, counterions conduct through the membrane, leading to a decrease in ion concentrations near the membrane as shown in Fig. 3, where ion concentrations are plotted for bias voltages $V = 1,4$.

Due to the wavy structure of the membrane surface, the electric field is distorted near the membrane. Within a wavelength, the electric field points towards the dip of the wave from both x and opposite-x directions. Action of the electric field upon the net space charge in the EDL generates an electric body force pulling fluid towards the dip. The resultant high pressure at the dip pushes fluid outwards from the membrane. Due to the fluid flow continuity, a vortex pair is formed above the wavy surface. These vortices are referred to as seed vortices. An example of the seed vortices is given in Fig. 4, where three vortex pairs (corresponding to three waves) at bias voltage $V = 4$ are displayed. Several features of the seed vortices are observed: (i) vortex width is defined

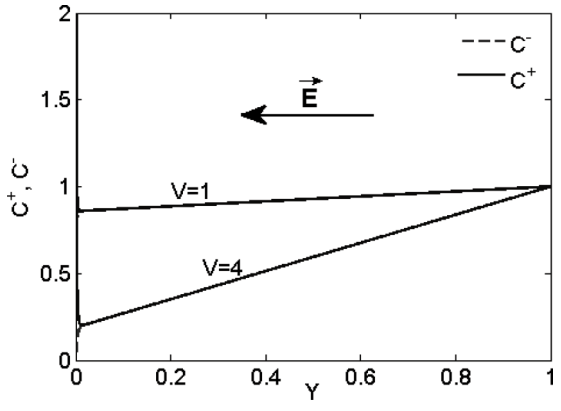

FIG. 3. Ion concentrations at bias voltages in Ohmic regime ($V = 1,4$). The electric field drives cations through the membrane, leading to decreases of ion concentrations near the membrane surface.

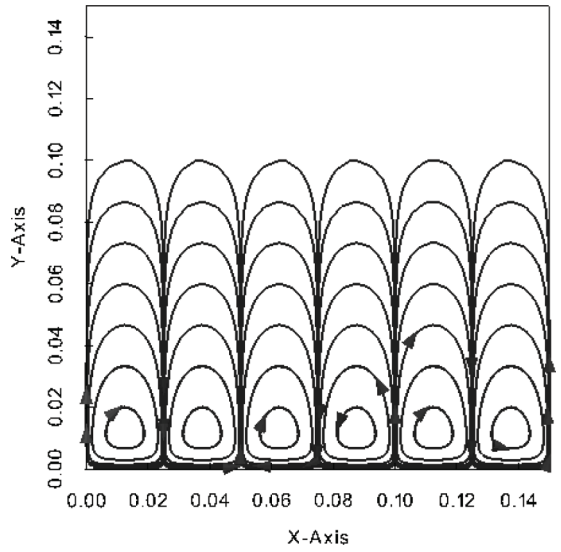

FIG. 4. Seed vortices in Ohmic regime ($V = 4$). The vortices are defined by the membrane structure (a,l). Due to the smallness of the surface perturbation, the flow velocity in the vortices is very low ($0.0015U_0$).

by the membrane structure, and is small compared to the system size; (ii) each vortex rotates in the opposite direction to its two neighbors as a result of the periodic wavy surfaces; (iii) maximum magnitude of flow velocity in the seed vortices is $\sim 0.0015U_0$, which is small due to the weak lateral electric field (determined by the bias voltage and the membrane structure) and small net charge in the EDL.

Due to the low flow velocity, the seed vortices contribute insignificantly into the overall transport of ions [through the convection term presented in Eq. (2)]. Ion transport in the system is dominated by diffusion, as shown in Fig. 3, where ion concentrations vary linearly with the distance from the membrane surface. When the bias voltage increases, the solution is more polarized at the membrane surface, as represented through the lowering ion concentrations near the membrane (Fig. 3). As a result, the gradient of ion concentration increases accordingly, producing an increasing diffusive flux which is proportional to the external electric field. The current therefore increases with the bias voltage manifesting the characteristic of the Ohmic regime (Fig. 14).

2. *Limiting-current regime—Development of extended space charge layer*

When bias voltage exceeds a critical value ($V_{cr1} = 7.5$), the concentration of ions near the membrane surface approaches zero. Beyond this critical value, a further increase in voltage insignificantly reduces the concentration near the membrane, but develops an extended space charge layer next to the EDL of the membrane. The extended space charge layer was first studied by Rubinstein and Shtilman [21], from the solution of a drift-diffusion equation under high electric field. It was demonstrated that, under such a condition, the equilibrium EDL becomes distorted, generating an extended space charge layer relating to the EDL but not part of it. Rather, it is a separate entity with minimal counterion concentration and near-zero co-ion concentration [22]. As shown in Fig. 5, the

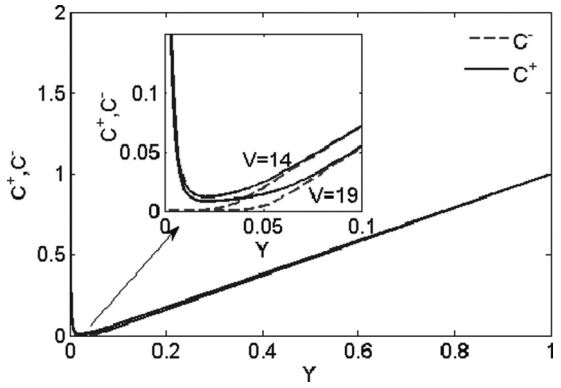

FIG. 5. Ion concentration at bias voltages in limiting regime $V = 14,19$. In this regime, ion concentration near the membrane approaches zero; a depletion zone develops near the membrane, and extends with increasing bias voltage.

thickness of the concentration polarization layer is ~ 0.05 (corresponding to bias voltage $V = 19$), which is much thicker than the original EDL (0.001). The extended space charge layers corresponding to bias voltages 4, 14, and 19 can also be inferred from plots of the space charge ($\rho_e = C_+ - C_-$) in Fig. 6. As can be seen, in the Ohmic regime ($V = 4$), the thickness of the space charge layer is only ~ 0.005 (in the order of the EDL thickness). In the limiting regime, the space charge layer is much thicker and can be extended up to 0.1 ($V = 19$).

Driven by electrical body force, fluid flow is determined by the electric field and the space charge. From Fig. 6, it shows that the space charge within the EDL in the limiting regime is higher than that in the Ohmic regime. The combined effect of a larger space charge and a stronger electric field generates a faster rotation of fluid in the seed vortices. Consequently, the vortices expand towards the bulk space as shown in Fig. 8(a), where each seed vortex at $V = 14$ has a height of 0.15, which is about two times higher than the seed vortex at $V = 4$ (Fig. 4).

Lateral velocities (U_x) in the Ohmic and limiting regimes are shown in Fig. 7. The lateral velocity in the limiting regime is approximately two times ($V = 19$) or three times ($V = 14$) larger than that in the Ohmic regime. However, the fluid flow is not strong enough to significantly alter the ion concentration,

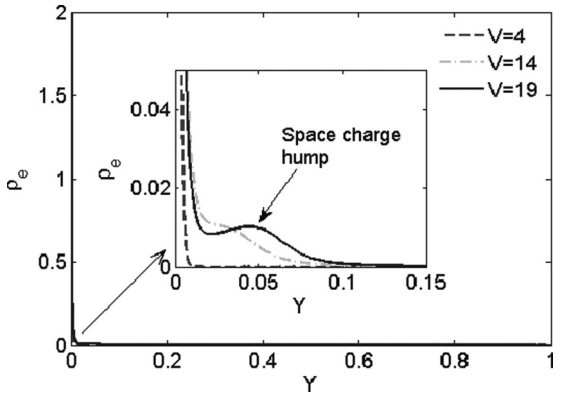

FIG. 6. Profile of space charge near the membrane in the Ohmic ($V = 4$) and limiting regimes ($V = 14$ and 19). Due to the development of an extended space charge layer, the space charge in the limiting regime is much greater than that in the Ohmic regime.

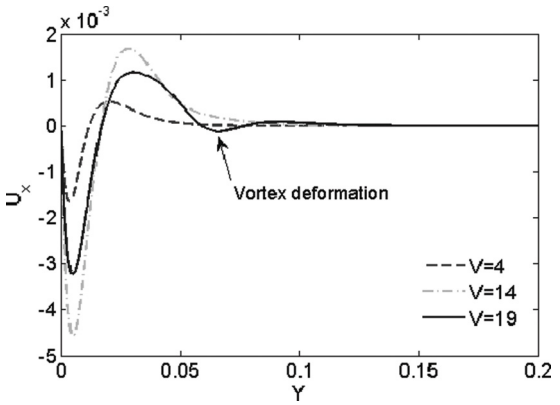

FIG. 7. Tangential velocity across a seed vortex at different bias voltages in the Ohmic ($V = 4$) and limiting regimes ($V = 14$ and 19). Action of an electric field on the extended space charge layer causes a deformation of seed vortices. The deformation is only significant at high bias voltages in the limiting-current regime (e.g., $V = 19$).

and its impact is still confined by the scale of membrane roughness. The ion concentrations are still uniform in the lateral direction. Due to the vanishing ion concentrations near the membrane, current passing through the membrane is only slightly increased for increasing voltages, corresponding to the limiting regime in the I-V curve (Fig. 14).

Action of the tangential electric field upon the extended space charge layer developing near a permselective surface was studied by Dukhin and co-workers [9]. They suggested a new kind of electro-osmosis flow, namely, electro-osmosis of the second kind, for a curved membrane surface. Subsequently, Rubinstein and Zaltzman advanced a theory of second kind electro-osmosis on a flat membrane surface [4]. It was shown that the second kind electro-osmosis can result in an instability of quiescent concentration polarization [3,4]. These studies represent the action of the tangential electric field upon the net charges in the extended space charge layer through the second kind electro-osmotic slip boundary conditions. In the present study, by solving the full set of governing equations, we are able to investigate the dynamics of the extended space charge layer and the effect of this dynamics on the fluid flow, as discussed in the following section.

3. *Effect of extended space charge layer on the fluid flow*

Due to the decrease in ion concentrations in the polarization layer, net space charge inside the EDL reduces at $V = 19$ compared to $V = 14$. The electrical body force inside the EDL at $V = 19$ is weakened accordingly. Consequently, the flow velocity at $V = 19$ is lower than that at $V = 14$, as shown in Fig. 7.

Although space charge in the EDL is lower, the extended space charge layer at $V = 19$ is thicker with the appearance of a space charge hump at position $y = 0.06$, as shown in Fig. 6. Action of the electric field on the extended space charge layer produces an effect on the flow in the layer. As seen from Fig. 8(a), this effect seems to be insignificant at $V = 14$. However, the effect becomes significant at $V = 19$, as shown in Fig. 8(b) where the vortices are deformed at a distance of $\sim$0.006 from the membrane. Compared with Fig. 6, we can see that the vortices are distorted at the position of the space charge hump in the extended space charge layer. Therefore, it can be stated that the development of extended space charge layers in the limiting-current regime tends to deform the seed vortices. The strength of this effect is determined by the space charge hump and the lateral electric field caused by the roughness of membrane surface.

A further increase in bias voltage generates a higher space charge hump and stronger lateral electric field; consequently, the deformation of the vortices is larger. When the voltage is significantly high, the seed vortices are broken; the vortices become unstable, leading to instability of the fluid flow.

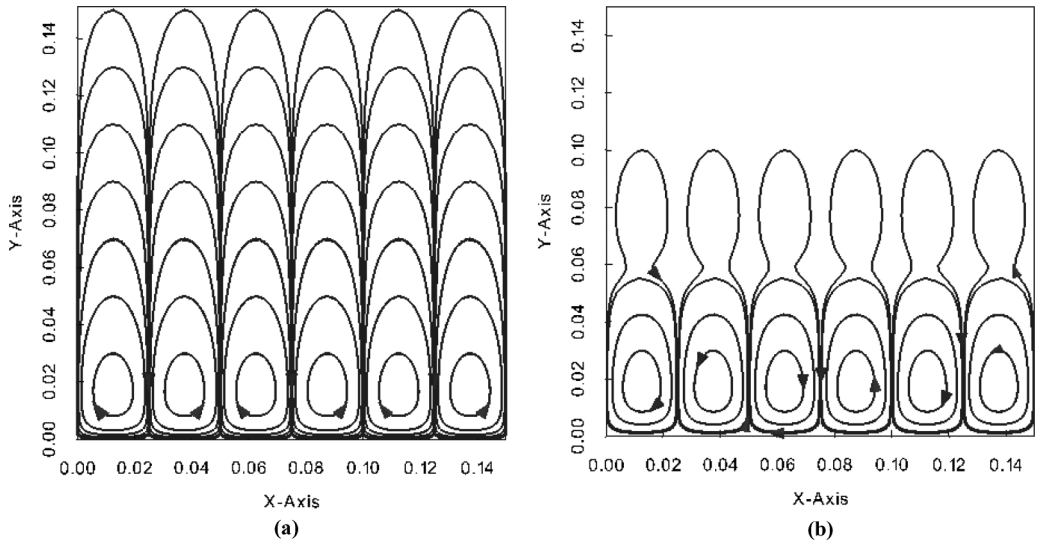

FIG. 8. Seed vortices in the limiting regime at $V = 14$ (a) and $V = 19$ (b). Due to the higher electric field, the seed vortices in the limiting regime are longer than those in the Ohmic regime (a). At high bias voltage in the limiting regime ($V = 19$), action of an electric field upon the extended space charge layer deforms the seed vortices at the location of space charge hump in the extended space charge layer (Fig. 6).

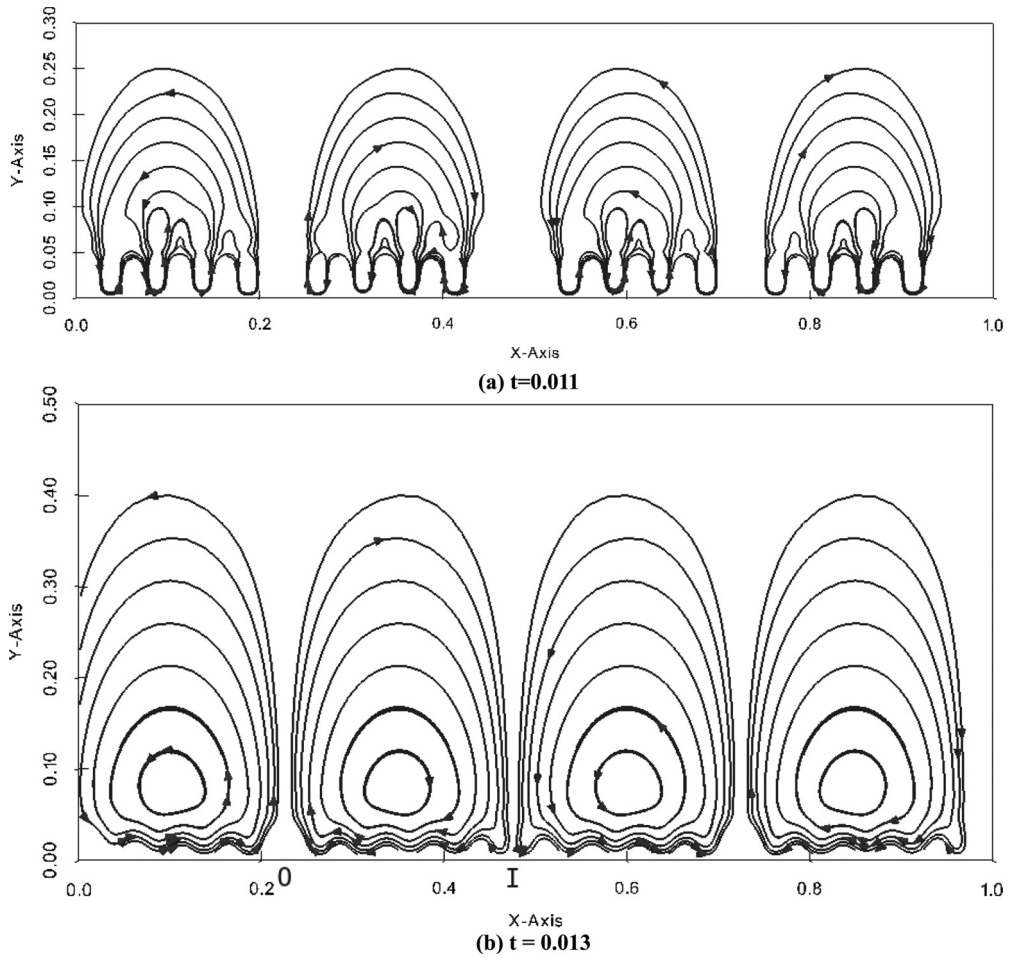

FIG. 9. Electroconvective instability at bias voltage $V = 22$. The action of an electric field on the extended space charge layer starts breaking the seed vortices from the top at $t = 0.011$ (a). Adjacent vortices merge to form a larger vortex; at $t = 0.013$, four large vortices are formed from the original 40 seed vortices (b).

4. Overlimiting current regime—Electroconvective instability

When the bias voltage exceeds a critical value ($V_{cr2} = 21$), the seed vortices are broken up by the deformation effect caused by the action of the electric field on the space charge in the extended space charge layer. In Fig. 9(a), the seed vortices start breaking up from their top at $t = 0.011$. At a time step later ($t = 0.013$), the original 40 seed vortices merge into four large vortices, which extend up to the position of $y = 0.4$ as

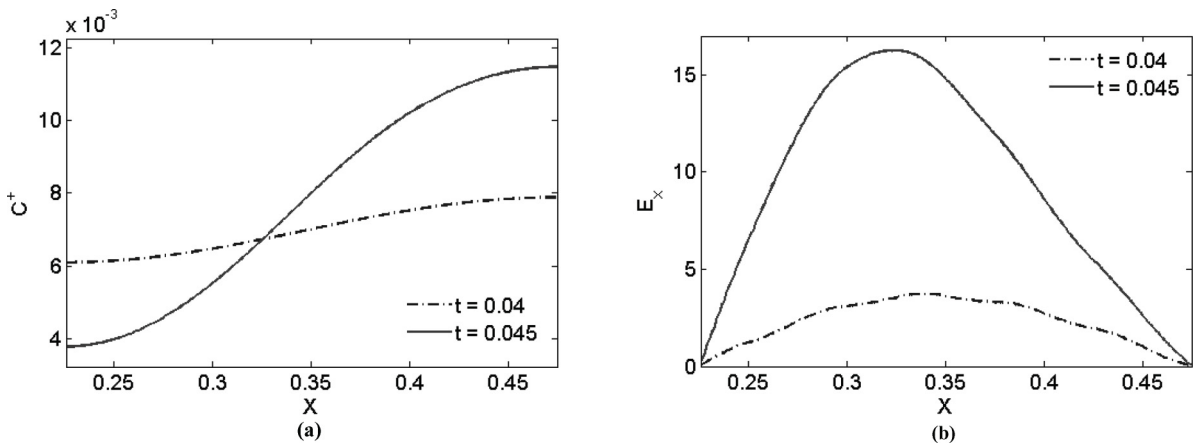

FIG. 10. The development in time of cation concentration (a) and lateral electric field (b) between I and O. The vortex causes an enhancement of ion concentration at I, where fluid is driven towards the membrane, and a depletion of ion concentration at O, where fluid is driven outwards from the membrane. Due to the concentration gradient between I and O, the lateral electric field is amplified in time.

shown in Fig. 9(b). Like the seed vortices, each large vortex rotates in a direction opposite to its adjacent vortices.

Due to the appearance of the large vortices, the fluid outside the depletion zone, which has high ion concentrations, is transported to the membrane surface. We investigate this transport process by considering the evolution in time of a single vortex determined by points O and I at coordinates $x_O = 0.225$ and $x_I = 0.475$ in Fig. 9(b). From the rotation direction (clockwise) of the vortex, we can see that the fluid, which has high ion concentrations, is driven to the membrane surface at the right side of the vortices (indicated by I). As a result, the ion concentrations are locally enhanced around I. The vortex, at the same time, returns the low ion concentration fluid on the membrane surface to the bulk space at the left side (indicated by O). It therefore expands the local depletion zone at O. The enhancement and depletion are shown in Fig. 10(a), where the cation concentration along the line connecting I and O at time steps 0.4 and 0.45 is plotted.

The concentration gradient between I and O produces an amplification to electric field [23], which strengthens the electric body force at the middle of I and O. The amplification is illustrated in Fig. 10, where the cation concentration and electric field at two time steps ($t = 0.04$ and $t = 0.045$) are plotted. As can be seen, the higher concentration gradient develops in time, and the stronger electric field is induced. This strong electric field tends to accelerate the flow velocity in the vortex.

In addition, the enhancement compresses the extended space charge layer at I; consequently, the space charge density in this layer is increased. The action of the vertical electric field on this high density space charge generates a high pressure at I. On the other hand, the depletion at O yields a decompression on the extended space charge layer resulting in a decrease in space charge density and related decrease in pressure. The compression and decompression on the extended space charge layer are depicted in Fig. 11(a), where the space charge layer at I is about a half narrower than that at O, and the space charge density at I is about two times higher. The related increase (at I) and decrease (at O) in pressure are shown in Fig. 11(b), where the pressure at I is about two times higher than that at O. The pressure drop between I and O also tends to accelerate the flow velocity in the vortex.

The combined effect of electric field amplification and pressure drop accelerating the rotation in the vortex is essentially a positive feedback and promotes electroconvective instability in the system. At steady state, the instability generates vortices in which fluid flow is accelerated to the speed of $130U_0$. This fast vortical flow transports ions to the membrane surface as can be seen in the contour plot of cation concentration in Fig. 12(b), where the ion concentration is the two-dimensional variation as opposed to the one-dimensional variation observed in the Ohmic and limiting regimes.

In order to understand the effect of the vortical flow on the ion transport, we compare the ion flux obtained with the vortical flow to the ion flux obtained without vortices (fluid flow is not considered in the system). A general form of ion flux is given by the Nernst-Planck equation (2):

$$\tilde{J}_{y+} = -\tilde{D}_+ \left(\frac{\partial \tilde{C}_+}{\partial \tilde{y}} + Z_+ \tilde{C}_+ \frac{\partial \tilde{\Phi}}{\partial \tilde{y}} \right) + \mathrm{Pe}\, \tilde{U}_y \tilde{C}_+. \qquad (9)$$

In the above equation, the first term is flux attributed to the ion diffusion, the second term is flux attributed to the field driven, and the last term is flux attributed to ion convection. In the no-vortices case, the last term in Eq. (9) is zero.

The comparison is presented in Fig. 13, where the components of cation flux passing though a cross section, which is 0.02 above the membrane surface, at $V = 22$ are plotted. Due to the impermeability to anions of the membrane, the anion flux is not shown. It is noted that the ion transport attributed to convection (crossed markers) is negligible because the cross section is very close to the membrane, which is impermeable to the fluid flow.

For the case without vortices, the ion flux components are uniform along the membrane surface manifesting the linear variation of ion concentrations and electric potential in the system. In addition, since the section is taken across the depletion layer, where cation concentration is low and flat

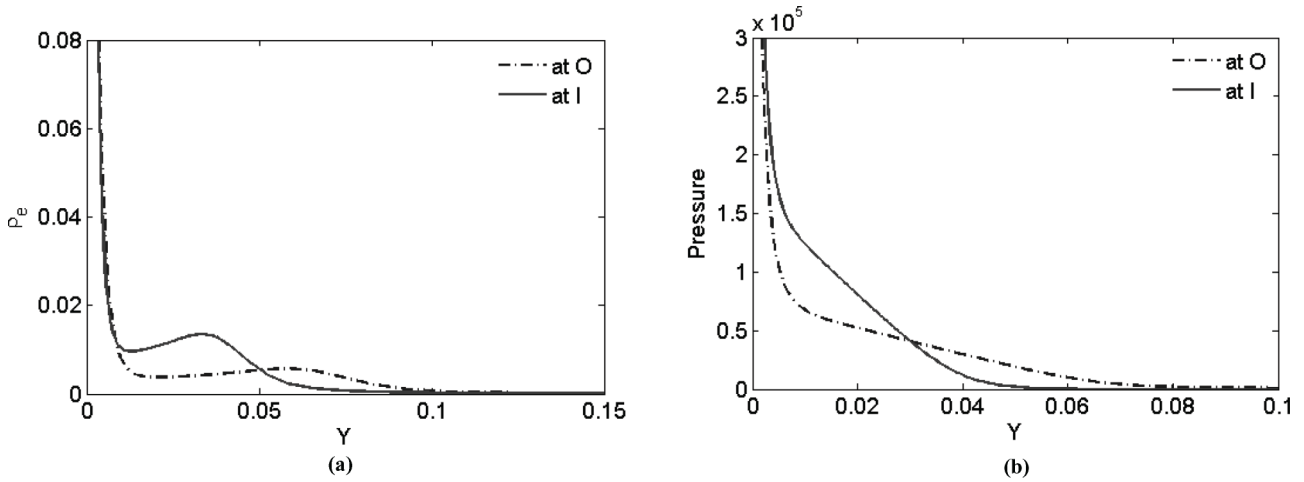

FIG. 11. Extended space charge layer (a) and pressure (b) at I and O. The coming in flow at I compresses the local extended space charge layer at I. In contrast, the coming out flow at O decompresses the local extended space charge layer at O. Action of a normal electric field on the unequal space charge densities at I and O causes a pressure gradient in the lateral direction which tends to speed up the vortex.

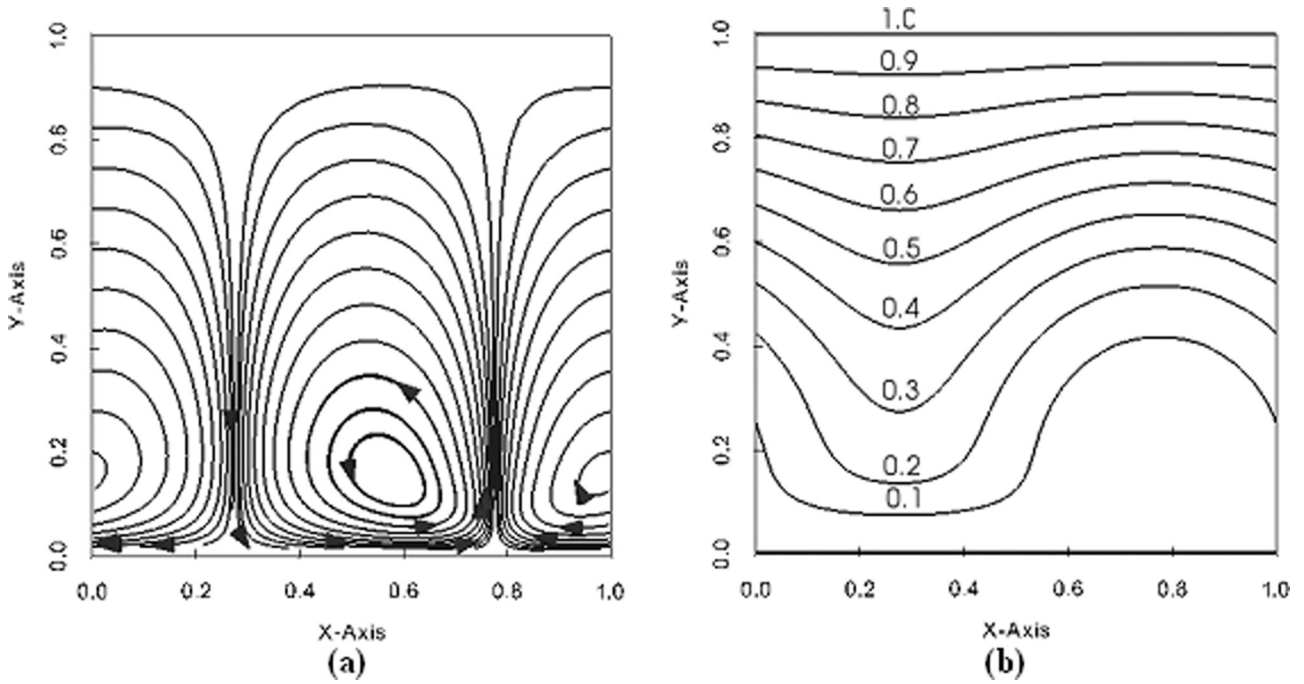

FIG. 12. The steady state streamlines (a) and contour lines of cation concentration (b) at $V = 22$. The vortices extend to the bulk space (a); the maximum flow velocity in the vortices is $130U_0$, which is much faster than that before the instability occurs. The vortices drive more ions to the membrane surface from one side and expand the depletion zone from the other side (b).

(Fig. 5), the flux component attributed to ion diffusion is negligible.

For the case with vortices in the region of enhanced ion concentration ($x = [0.0, 0.6]$), the flux components attributed to diffusion and field driven are much higher than those in the no-vortices case. On the other hand, the expansion of the depletion zone reduces the local conductivity. As a result, the flux components in the depletion zone ($x = 0.6$–0.95) decrease to lower than those in the no-vortices case. However, due to the larger amount of enhanced current, the overall current in the vortices case is higher than that (the limiting current) in the no-vortices case.

Due to the instability, higher bias voltage results in a faster flow velocity in the vortices. The faster flow carries more ions

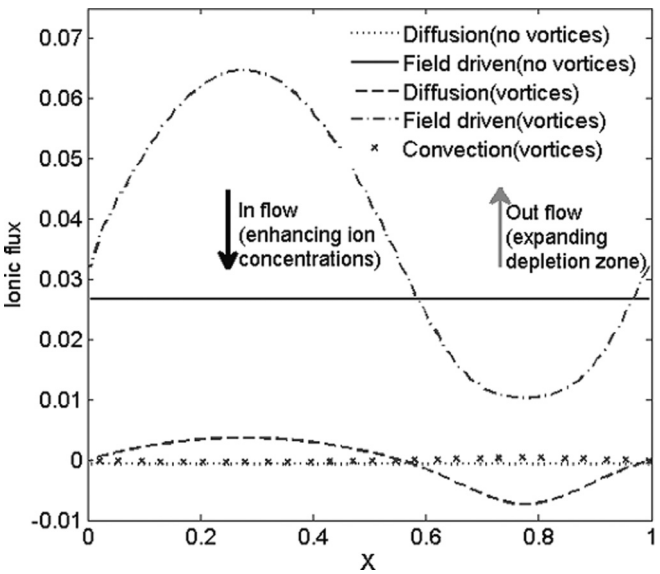

FIG. 13. Flux components in the vortices case is compared with the no-vortices case. In the region $x = [0,0.6]$, where ion concentrations are enhanced by the coming in flow, flux components attributed to the diffusion and field driven are much higher than those in the no-vortices case. In contrast, in the region $x = [0.6,0.95]$, where coming out flow expands the depletion zone, the flux components are lower than those in the no-vortices case. Because the enhanced fluxes are larger than the reduced fluxes, the total current passing through the membrane increases over the limiting-current value.

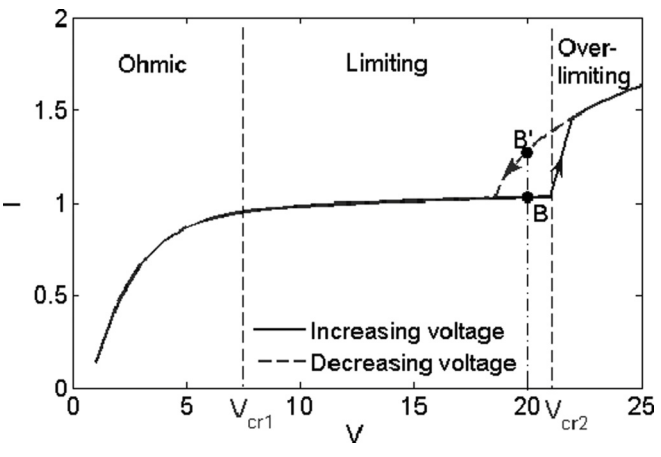

FIG. 14. Current-voltage (I-V) curve for the permselective membrane obtained by increasing bias voltages (solid line) and by decreasing bias voltages (dashed line). In the I-V curves, three regimes are identified: Ohmic, limiting, and overlimiting. The nonoverlapping I-V curves at the transition between limiting and overlimiting current regimes exhibit a hysteretic behavior of the electric current.

to the membrane surface to enhance the solution conductivity. Therefore, beyond the limiting-current regime, the current increases again with the increasing bias voltage, creating the overlimiting current regime in the I-V curve (Fig. 14).

As discussed above, the instability is caused by the action of the lateral field upon the extended space charge layer. Since the lateral field increases with roughness of the membrane surface, larger wave amplitude (a) will induce stronger lateral field. Hence, an increase in the wave amplitude of the membrane surface leads to an earlier onset of the instability, and so the overlimiting current regime. This is consistent with the conclusions of Rubinstein and Zaltzman [4] and Balster *et al*. [24] on the influence of membrane surface heterogeneity on the length of the limiting-current region.

Currents passing through the membrane at different bias voltages are collected to form the voltage-current (I-V) curve shown in Fig. 14. In the I-V curve, three regimes are identified. First, the Ohmic regime, where the convection flow is negligible, an increase in applied voltage results in a reduction of ion concentration near the membrane and an increase in current. Secondly, the limiting-current regime, which is characterized by the almost constant current with increasing bias voltage, the saturated current is due to the vanishing of ions at the membrane-solution interface. The last regime is the overlimiting current regime occurring at high bias voltages. In this regime, solution conductivity is increased significantly due to strong vortical flow caused by electroconvective instability.

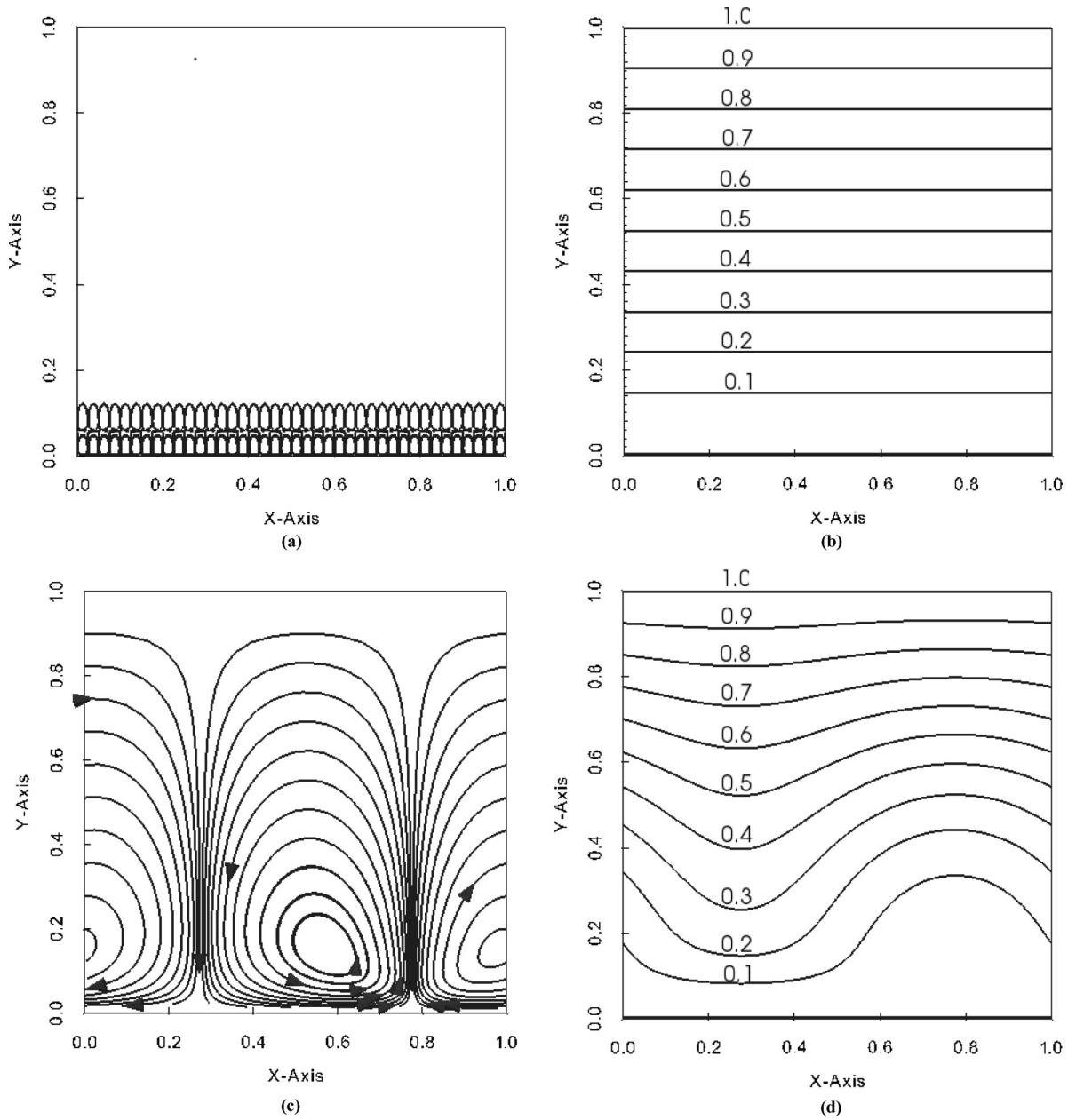

FIG. 15. Steady state streamlines and contour lines of cation concentration at B [(a), (b)] and B′ [(c), (d)]. Due to the initial vortices and depletion zone, at the same bias voltage the fluid flow and ion concentration at B′ are different from those at B. The large vortices at B′ transport more ions to the membrane surface, thus enhancing current passing through the membrane.

B. Hysteretic behavior

As described in the previous section, when the bias voltage increases, there is a critical voltage which acts as a threshold between the limiting and overlimiting current regimes. At the critical voltage, the seed vortices are broken up to form large vortices. The process of merging vortices involves a large scale change in the flow field, and modifies the mode of ion transport. It is interesting to study the reversibility of this process, i.e., whether the system exhibits the same behavior when the bias voltage is decreased passing the critical region.

For this purpose, the system is solved for decreasing bias voltages starting from a voltage in the overlimiting current regime. Ionic currents obtained are plotted in Fig. 14 along with the I-V curve obtained with increasing voltages. It is obvious that the I-V curves do not coincide with each other at the transition between limiting and overlimiting current regimes indicating a hysteretic behavior of the current at the transition.

In order to investigate the mechanism behind the hysteretic behavior, we consider flow fields at increasing and decreasing bias voltage $V = 20$ denoted by points B and B′ in Fig. 14. The flow field at B, shown in Fig. 15(a), features a limiting conductance regime with a series of small vortices defined by the membrane surface structure. In contrast, the flow field at B′, shown in Fig. 15(c), consists of two large vortices. It is shown from Figs. 12(a) and 15(c) that the flow pattern at B′ is similar to that at the overlimiting current regime; the flows are different only in flow velocity magnitude.

The maintenance of overlimiting current flow pattern at a voltage below the critical value can be explained by the existing vortical flow and depletion zone. The bias voltage ($V = 20$) induces a large pressure in the extended space charge layer of the membrane. Due to the lateral balance in the system at B, the pressure pushes fluid perpendicularly onto the membrane surface instead of driving a lateral fluid flow. In contrast, at B′, the vortical flow resulting from electroconvective instability compresses the extended space charge region of membrane from one side (coming in flow), and decompresses it from the other side (coming out flow). Consequently, it raises a lateral difference of pressure on the membrane surface. Therefore, the high pressure in the extended space charge layer is invoked to retain the vortical flow. Furthermore, the slight lateral electric field caused by the surface perturbation is not able to drive a macroscopic flow in the system at B. In contrast, at B′, the existing depletion zone produces a lateral concentration gradient which generates a high lateral electric field. Consequently, it produces an additional lateral body force to retain the vortical flow. A comparison between lateral electric fields at B and B′ is shown in Fig. 16. As can be seen from the figure, the electric field at B is defined by structure of the membrane surface manifested by the short wavelength curve. The electric field profile at B′ is a combination of two components: a short wavelength component defined by the membrane structure and a long wavelength component caused by the lateral concentration gradient across the depletion zone.

When voltage decreases further, the rotation velocity reduces accordingly; the factors retaining the large vortices flow (including the lateral pressure gradient and the lateral concentration gradient) are weakened accordingly. Eventually, the system returns to the state with seed vortices, and the ion transport is dominated again by ion diffusion (Fig. 14).

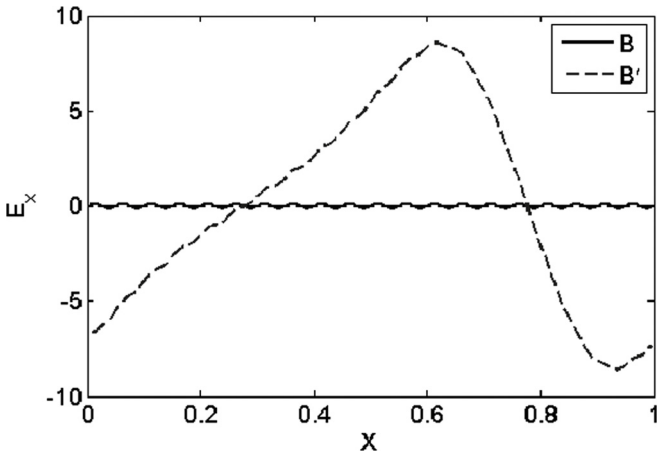

FIG. 16. Lateral electric fields near the membrane surface at B (solid line) and B′ (dashed line). Due to the nonuniform depletion zone, the lateral electric field at B′ is much larger than that at B. The lateral body force caused by the large electric field helps to maintain the overlimiting current flow pattern at B′.

The hysteretic behavior indicates an important role of vortical flow in the overlimiting current regime. This flow mixes the diffusion layer to bring high concentration fluid to the membrane and form depletion zones. Thus, lateral electric field and pressure gradient are generated to maintain the vortical flow at a voltage below the critical value.

V. CONCLUSION

By solving the coupled Poisson-Nernst-Planck-Navier-Stokes equations, we obtain direct numerical solution for the nonlinear electrokinetic flow near the permselective membrane. The solution demonstrates the occurrence of electroconvective instability at a significantly high voltage as a result of the action of an electric field on the extended space charge layer. We clarify the mechanism behind the change of conductivity in an I-V curve. The vortical flow resulting from the instability transports more ions to the membrane to promote an overlimiting current passing through it. More importantly, we observe a hysteretic behavior of current in the transition between a limiting and an overlimiting regime. The hysteretic behavior is characterized by the significant difference between flow pattern and ion distribution in limiting and overlimiting regimes. The role of electroconvective instability is exhibited through the hysteresis: Once the ion concentrations are redistributed by the vortical flow, the resultant macroscopic lateral electric field and pressure gradient are able to maintain the overlimiting current regime at a voltage below the critical value.

ACKNOWLEDGMENTS

This work was funded by SMA-II CE Programme Flagship research project, as well as SMART Centre (BioSyM IRG). We also thank Dr. Boris Zaltzman (Ben Gurion University, Israel) for his helpful recommendations.

[1] V. G. Levich, *Physicochemical Hydrodynamics* (Prentice-Hall, Englewood Cliffs, NJ, 1962).
[2] H. C. Chang and G. Yossifon, Biomicrofluidics **3**, 012001 (2009).
[3] I. Rubinstein and B. Zaltzman, Math. Models Meth. Appl. Sci. **6**, 623 (1999).
[4] I. Rubinstein and B. Zaltzman, Phys. Rev. E **62**, 2238 (2000).
[5] S. J. Kim, Y. C. Wang, J. H. Lee, H. Jang, and J. Han, Phys. Rev. Lett. **99**, 044501 (2007).
[6] S. M. Rubinstein, G. Manukyan, A. Staicu, I. Rubinstein, B. Zaltzman, R. G. H. Lammertink, F. Mugele, and M. Wessling, Phys. Rev. Lett. **101**, 236101 (2008).
[7] G. Yossifon and H. C. Chang, Phys. Rev. Lett. **101**, 254501 (2008).
[8] F. Maletzki, H. W. Rosler, and E. J. Staude, J. Membr. Sci. **71**, 105 (1992).
[9] S. S. Dukhin, Adv. Colloid Interface Sci. **35**, 173 (1991).
[10] E. A. Demekhin, V. S. Shelistov, and S. V. Polyanskikh, Phys. Rev. E **84**, 036318 (2011).
[11] A. Prhol and M. Schmuck, M2AN Math. Model. Numer. Anal. **44**, 531 (2010).
[12] M. Darwish, I. Sraj, and F. Moufalled, J. Comput. Phys. **288**, 180 (2009).
[13] C. M. Rhie and W. L. Chow, AIAA J. **21**, 1525 (1983).
[14] J. H. Ferziger and M. Peric, *Computational Methods for Fluid Dynamics*, 3rd ed. (Springer, 2001).
[15] J. E. Dennis, Jr. and R. B. Schnabel, *Numerical Methods for Unconstrained Optimization and Nonlinear Equations* (Prentice-Hall, Englewood Cliffs, NJ, 1983).
[16] C. Geuzaine and J. F. Remacle, Comput. Methods Appl. Mech. Eng. **79**, 1309 (2009).
[17] Y. Saad and M. H. Schultz, SIAM J. Sci. Stat. Comput. **7**, 856 (1986).
[18] S. Balay, J. Brown, K. Buschelman, V. Eijkhout, W. Gropp, D. Kaushik, M. Knepley, L. Curfman McInnes, B. Smith, and H. Zhang, PETSc Users Manual, ANL-95/11 - Revision 3.1.8 (Argonne National Laboratory, Mathematics and Computer Science Division, Argonne, IL, 2010).
[19] V. S. Pham, Ph.D. thesis, National University of Singapore, Singapore, 2012.
[20] C. M. Rhie and W. L. Chow, AIAA J. **21**, 1525 (1983).
[21] I. Rubinstein and L. Shtilman, J. Chem. Soc., Faraday Trans. 2 **75**, 231 (1979).
[22] I. Rubinstein and B. Zaltzman, Phys. Rev. E **81**, 061502 (2010).
[23] S. J. Kim, L. Li, and J. Han, Langmuir **25**, 7759 (2009).
[24] J. Balster, M. H. Yildirim, D. F. Stamatialis, R. Ibanez, R. G. H. Lammertink, V. Jordan, and M. Wessling, J. Phys. Chem. B **111**, 2152 (2007).